Exploration of Mixed-metal Polyoxometalate derivatives towards Electrochemical Energy Storage Applications

Dissertation submitted to
Visvesvaraya National Institute of Technology, Nagpur
in partial fulfillment of the requirements for the award of
the degree

Master of Science
in
Chemistry

by

Devanshi Shukla (MS23CHM003)

under the guidance of

Dr. Abhishek Banerjee

Department of
Visvesvaraya National Institute of Technology
Nagpur 440010 (India)

2025

Exploration of Mixed-metal Polyoxometalate derivatives towards Electrochemical Energy Storage Applications

Dissertation submitted to
Visvesvaraya National Institute of Technology, Nagpur
in partial fulfillment of the requirements for the award of
the degree

Master of Science

in

Chemistry

by

Devanshi Shukla (MS23CHM003)

under the guidance of

Dr. Abhishek Banerjee

Visvesvaraya National Institute of Technology

Nagpur 440010 (India)

2025

© Visvesvaraya National Institute of Technology (VNIT) 2009

Department of Chemistry

Visvesvaraya National Institute of Technology, Nagpur

Declaration

I, Devanshi Shukla, hereby declare that this dissertation titled "**Exploration of Mixed-metal Polyoxometalate derivatives towards Electrochemical Energy Storage Applications**" is carried out by me in the Department of Chemistry of Visvesvaraya National Institute of Technology, Nagpur. The work is original and has not been submitted earlier, whole or in part, for the award of any degree/diploma at this or any other Institution / University.

Date:

Certificate

This to certify that the dissertation titled "**Exploration of Mixed-metal Polyoxometalate derivatives towards Electrochemical Energy Storage Applications**" is submitted by **Devanshi Shukla** in partial fulfillment of the requirements for the award of the degree of **Master of Science in Chemistry**, VNIT Nagpur. The work is comprehensive, complete and fit for final evaluation.

Dr. Abhishek Banerjee
Assistant Professor
Department of Chemistry
VNIT, Nagpur

Head of the Department,
Department of Chemistry,
VNIT, Nagpur.
Date:

Non-Plagiarism Certificate

It is certified that the M.Sc. dissertation titled "**Exploration of Mixed-metal Polyoxometalate derivatives towards Electrochemical Energy Storage Applications**" by **Devanshi Shukla** bearing Enrollment No. MS23CHM003, ID- 30109 has been examined by us with the following anti-plagiarism tools.

The thesis has been checked using TURNITIN (copy of originality report attached) and found within limits as per HEC plagiarism Policy and instructions issued from time to time.

Devanshi Shukla

MS22CHM003

Dr. Abhishek Banerjee

Assistant Professor

Department of Chemistry

VNIT, Nagpur 440010

Acknowledgement

I would like to express my heartfelt gratitude to everyone who contributed to the success of this project.

Firstly, I am deeply thankful to my supervisor, Dr. Abhishek Banerjee, whose guidance, constant motivation, and support were invaluable throughout this period. His genuine interest and invaluable advice were crucial to my progress.

I am also profoundly grateful to the Head of the Department, Dr. Sujit K. Ghosh, for his dedication to science and research and for providing all necessary facilities until the end of this research.

I acknowledge the Oxo-Thiometalate Lab, Dept of Chemistry, VNIT Nagpur, for their support in completing this project. Special thanks to the PhD scholars, Kalyan Morla, Shikha Singh, Sandeep Chaudhary, and my labmate Sneha Mishra, for their technical assistance and for nurturing me with their mental and moral support. I am forever indebted to them.

I appreciate my colleagues and fellow mates for their collaboration, stimulating discussions, and camaraderie. Their constructive criticisms and shared knowledge guided me through this journey.

Lastly, I want to express my heartfelt gratitude to my family for their unwavering support, belief, and blessings throughout my life. I am also grateful to the Almighty for giving me the strength to persevere through this time.

Abstract

Polyoxometalates (POMs), composed of early transition metals in high oxidation states, possess robust structures ideal for demanding applications such as continuous electrochemical charge-discharge cycles. With growing renewable energy use, the development of newer materials enabling rapid energy storage and release has become increasingly important. Energy storage systems operate via Faradaic (batteries) or Electrostatic (capacitors) mechanisms, which represent extremes in the energy and power density spectrum. Supercapacitors bridge this gap, offering fast charge-discharge accompanied by high-power output. This research explores mixed-metal POMs – specifically vanado-molybdates and vanado-tungstates, for their potential in advanced energy storage, aiming to combine structural stability with enhanced electrochemical performance.

Electrochemical energy storage studies were conducted on vanado-molybdate $H_6[PV_3Mo_9O_{40}]$ and vanado-tungstate $(NH_4)_6H[PV_4W_8O_{40}]$, both Keggin-type derivatives; and compared with their respective non-vanadium analogues, $H_3[PMo_{12}O_{40}]$ and $H_3[PW_{12}O_{40}]$, respectively. Cyclic voltammetry, galvanostatic charge–discharge, and electrochemical impedance spectroscopy were employed to evaluate charge-storage behavior and stability.

As anticipated, vanadium-containing derivatives demonstrated enhanced capacitance; in comparison with the non-vanadium compounds, ostensibly due to their fully oxidized states and limited redox reversibility, hindering efficient electron transfer. For $H_6[PV_3Mo_9O_{40}]$ and $(NH_4)_6H[PV_4W_8O_{40}]$, significantly improved areal capacitance with values of 7.75 and 7.64 mF/cm^2 at a scan rate of 100mV/s was observed, respectively. In comparison, the non-vanadium analogues for $H_3[PMo_{12}O_{40}]$ and $H_3[PW_{12}O_{40}]$ showed aerial capacitance values of 4.18 and 6.89 mF/cm^2, respectively, at the same scan rate. This improvement in electrochemical performance is attributed to vanadium's accessible multiple oxidation states (+3, +4, +5), which facilitate rapid Faradaic redox processes at the electrode–electrolyte interface. The redox reactions, involving direct electron transfer, significantly contribute to the overall charge storage capability, resulting in higher specific capacitance of $H_6[PV_3Mo_9O_{40}]$ and $(NH_4)_6H[PV_4W_8O_{40}]$. Thus, incorporation of vanadium into the Keggin framework effectively enhances electrochemical performance, making such materials promising candidates for high-rate supercapacitor applications.

List of Figures

Figure Caption	Page No.
Figure 1.1: Schematic illustration of a battery	**3**
Figure 1.2: Schematic of an electrostatic capacitor	**4**
Figure 1.3: Schematic illustration of a supercapacitor	**6**
Figure 1.4: Ragone plot for various energy storage devices	**7**
Figure 1.5: Current Energy Storage Systems: State of the Art	**8**
Figure 1.6: Classification of supercapacitors and related electrode materials	**10**
Figure 1.7: Electrochemical Double Layer Capacitor (EDLC)	**11**
Figure 1.8: Pseudocapacitor	**11**
Figure 1.9: Hybrid-type supercapacitor	**12**
Figure 1.10: Polyhedral representation of some common isopolyanions and heteropolyanions	**13**
Figure 1.11: Scheme highlighting the fact that discrete POMs are in between $[MO_4]^{n-}$ and mono-extended solid oxides. The controlled acidification of a solution of $[MO_4]^{n-}$ leads to the formation of discrete structure POMs	**14**
Figure 2.1: Fabrication of the electrode	**22**
Figure 2.2: Three-electrode system	**23**
Figure 3.1: Polyhedral representation of $[PW_{12}O_{40}]^{3-}$ vs. $[PV_4W_8O_{40}]^{7-}$, and $[PMo_{12}O_{40}]_{3-}$ vs. $[PV_3Mo_9O_{40}]^{6-}$. Color code: Green polyhedra – $\{WO_6\}$, Dark blue polyhedra – $\{MoO_6\}$, Orange polyhedra – $\{VO_6\}$, Magenta polyhedral – $\{PO_4\}$.	**26**
Figure 3.2: PXRD Data of the synthesized materials	**27**
Figure 3.3: Infrared Spectra	**28**
Figure 3.4: UV-Visible spectra of $H_3[PW_{12}O_{40}]$, and $(NH_4)_6H[PV_4W_8O_{40}]$	**29**
Figure 3.5: UV-Visible spectra of $H_3[PMo_{12}O_{40}]$, and $H_6[PV_3Mo_9O_{40}]$	**30**
Figure 3.6: CV Curve for $(NH_4)_6H[PV_4W_8O_{40}]$	**31**
Figure 3.7: CV Curve for $H_6[PV_3Mo_9O_{40}]$	**32**
Figure 3.8: Cyclic Voltammetry comparison between $(NH_4)_6H[PV_4W_8O_{40}]$ and $H_3[PW_{12}O_{40}]$	**33**

Figure 3.9: Cyclic Voltammetry comparison between $H_6[PV_3Mo_9O_{40}]$ and $H_3[PMo_{12}O_{40}]$	**34**
Figure 3.10: GCD Curve for $(NH_4)_6H[PV_4W_8O_{40}]$	**35**
Figure 3.11: GCD Curve for $H_6[PV_3Mo_9O_{40}]$	**36**
Figure 3.12: a) Nyquist Plot and b) Bode Plot for $(NH_4)_6H[PV_4W_8O_{40}]$	**37**
Figure 3.13: a) Nyquist Plot and b) Bode Plot for $H_6[PV_3Mo_9O_{40}]$	**37**

List of Tables

Table Caption	Page No.
Table 1.1: Comparison of capacitors, batteries, fuel cells, and supercapacitors	**9**
Table 3.1: Areal capacitance values for $(NH_4)_6H[PV_4W_8O_{40}]$	**31**
Table 3.2: Areal capacitance values for $H_6[PV_3Mo_9O_{40}]$	**32**
Table 3.3: Calculation of areal capacitance for $(NH_4)_6H[PV_4W_8O_{40}]$	**35**
Table 3.4: Calculation of areal capacitance for $H_6[PV_3Mo_9O_{40}]$	**36**

Abbreviations

POM	Polyoxometalate
POV	Polyoxovandate
HOMO	Highest Occupied Molecular Orbital
LUMO	Lowest Occupied Molecular Orbital
EDLC	Electrochemical Double Layer Capacitor
UV-Vis	Ultraviolet-Visible
FTIR	Fourier Transform Infrared Spectroscopy
P-XRD	Powder X-ray Diffraction
CV	Cyclic Voltammetry
GCD	Galvanic Charge Discharge
EIS	Electrochemical Impedance Spectroscopy
SC	Supercapacitor
HCl	Hydrochloric Acid

Contents

Abstract vi
List of Figures vii
List of Tables ix
Abbreviations x
CHAPTER 1: INTRODUCTION 1
1.1 Types of Energy Storage Devices 3
1.1.1 Batteries 3
1.1.2 Capacitors 4
1.1.3 Supercapacitors 6
1.2 Comparison between energy storage devices 7
1.3 Types of supercapacitors and their working mechanism 9
1.3.1 Electrochemical Double Layer Capacitors (EDLC) 10
1.3.2 Pseudocapacitors 11
1.2.3 Hybrid Supercapacitor 12
1.4 Polyoxometalates (POMs) 12
1.3.1 Structural types in Polyoxometalates (POMs) 13
1.3.2 Synthesis Strategies 14
1.3.3 Formation of Polyoxotungstates and Polyoxomolybdates 15
1.5 Utility of POMs in the development of supercapacitors 15
1.6 Perspective of current work 16
CHAPTER 2: SYNTHESIS, CHARACTERIZATION AND METHODOLOGIES 18
2.1 Synthesis 19
2.1.1 Phosphotungstic acid: $H_3[PW_{12}O_{40}]$ 19
2.1.2 Phosphomolybdic acid: $H_3[PMo_{12}O_{40}]$ 19
2.1.3 Vanado-Tungstate derivative: $(NH_4)_6H[PV_4W_8O_{40}]$ 20
2.1.4 Vanado-Molybdate derivative: $H_6[PV_3Mo_9O_{40}]$ 20
2.2 Characterization Techniques 21
2.2.1 Powder X-ray diffraction (P-XRD) 21
2.2.2 Fourier transform infrared (FT-IR) spectroscopy 21
2.2.3 Optical Spectroscopy 21
2.3 Fabrication of Electrodes by Doctor Blade Technique 21
2.4 Electrochemical Studies: Supercapacitive Properties 23
2.4.1 Cyclic Voltammetry 23
2.4.2 Galvanostatic Charge Discharge 24

2.4.3 Electrochemical Impedance Spectroscopy 24
CHAPTER 3: RESULTS AND DISCUSSION 25
3.1 Structure of synthesized compounds 26
3.2 Characterization of synthesized compounds 26
3.2.1 Powder X-ray Diffraction 26
3.2.2 Infrared Spectroscopic Studies 27
3.2.3 UV-Visible spectroscopy 28
3.3 Electrochemical Studies 30
3.3.1 Cyclic Voltammetry 30
a) $(NH_4)_6H[PV_4W_8O_{40}]$ 30
b) $H_6[PV_3Mo_9O_{40}]$ 31
c) Comparison between $(NH_4)_6H[PV_4W_8O_{40}]$ and $H_3[PW_{12}O_{40}]$ 32
d) Comparison between $H_6[PV_3Mo_9O_{40}]$ and $H_3[PMo_{12}O_{40}]$ 33
3.3.2 Galvanostatic charge discharge studies 34
a) $(NH_4)_6H[PV_4W_8O_{40}]$ 34
b) $H_6[PV_3Mo_9O_{40}]$ 35
3.3.3 Electrochemical Impedance Spectroscopic studies 36
a) $(NH_4)_6H[PV_4W_8O_{40}]$ 36
b) $H_6[PV_3Mo_9O_{40}]$ 37
CHAPTER 4: CONCLUSION 38

CHAPTER 1: INTRODUCTION

1. INTRODUCTION

With the increasing necessity towards creating sustainable energy sources, there is also an increasing need towards more efficient energy storage systems. Despite significant advancements in high-performance lithium-ion batteries and fuel cells, their limitations, such as poor power capability and high maintenance costs, have restricted their use in many applications [1]. However, supercapacitors have recently gained significant attention due to their exceptional properties, including rapid charge and discharge rates, long lifespan, high power density and safety features, that eliminate the risk of short circuits associated with traditional batteries and fuel cells [2].

Currently, the three leading commercially used energy storage technologies include capacitors, batteries, and fuel cells. To better understand the features of all three energy storage systems; and elucidate the advantages that supercapacitors offer, the following sections of this chapter will examine and compare their structures, working principles, and performance characteristics with those of the other devices [3].

Supercapacitors, also known as ultracapacitors or electrochemical capacitors, store energy through two primary mechanisms: electric double layer capacitance, which relies on ion adsorption, and pseudocapacitance, which is driven by surface redox reactions. While pseudocapacitors, which mostly utilize conducting polymers or metal oxides as electrode materials, demonstrate impressive capacitive performance, they often struggle to maintain this performance over extended cycling [4]. In contrast, electric double-layer (EDL) capacitors can endure up to a million charge-discharge cycles without any significant decline in performance. Additionally, because ion transport in EDL capacitors is faster than the redox reactions in other systems, they offer superior charge-discharge rates and power density. However, their energy density remains relatively low—typically around 3–5 Wh/kg—compared to commercial lithium-ion batteries, which range from 100 to 275 Wh/kg. As a result, one of the key challenges in supercapacitor research today is how to enhance their energy storage capacity without substantially compromising power output [5] [6].

1.1 Types of Energy Storage Devices

In this section we will discuss the different types of energy storage devices and their features.

1.1.1 Batteries

Batteries have become the most widely used power source across a broad range of industrial and consumer electronic devices. They operate by converting stored chemical energy into electrical energy through redox (reduction-oxidation) reactions. A standard battery is made up of one or more electrochemical cells, each consisting of two electrodes connected through an electrolyte that allows the movement of both anions (negatively charged ions) and cations (positively charged ions) [**Figure 1.1**]. The direction in which these ions move determines the polarity of the cell. During charging, the electrode where anions move is known as the anode (negative electrode), while the one receiving cations is referred to as the cathode (positive electrode). In general, energy is released in batteries through redox reactions, where cations are reduced at the cathode and anions are oxidized at the anode [7].

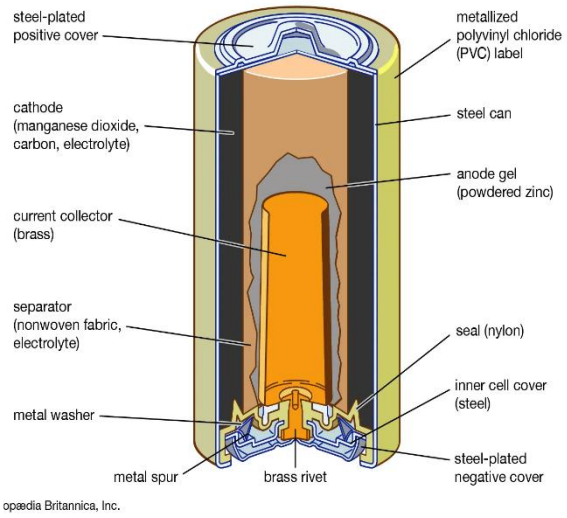

Figure 1.1: Schematic illustration of a battery

Based on their ability to be recharged, batteries can be categorized into two main types: **primary (non-rechargeable)** and **secondary (rechargeable) batteries**. Typically, non-rechargeable batteries offer higher energy density compared to their rechargeable counterparts.

In a standard battery, the anode is usually composed of graphite or other carbon-based materials, while the cathode consists of compounds such as lithium cobalt oxide, manganese oxide, or nickel-based oxides. Cation shuttle between the two electrodes during operation. When the battery is charging, ions migrate and embed themselves into the graphite anode. Upon discharging, and when the battery is connected to a load, the ions return to the cathode [8]. At present, batteries are considered among the most advanced electrochemical energy storage systems, offering a high energy density in the range of 120–170 Wh/kg. They are relatively lightweight and benefit from having no memory effect, making them highly suitable for a wide range of applications. However, despite their excellent specific energy, lithium-ion batteries and similar technologies often face limitations in terms of power output, as they typically have slower charge and discharge rates.

1.1.2 Capacitors

A capacitor is a passive component used in electrical systems to store energy in the form of an electric charge, which is held within the electric field between two conductive plates known as electrodes. Standard or electrostatic capacitors consist of two conductive plates separated by an insulating material called a dielectric, as illustrated in **Figure 1.2**. When a voltage is applied across the electrodes, opposite charges build up on each plate. Since the dielectric prevents direct current flow, an electric field forms between the plates, enabling the capacitor to store energy [9]. Although capacitors are capable of delivering energy very quickly, making them useful for high-power applications. Although, the amount of energy they can store is relatively small [10].

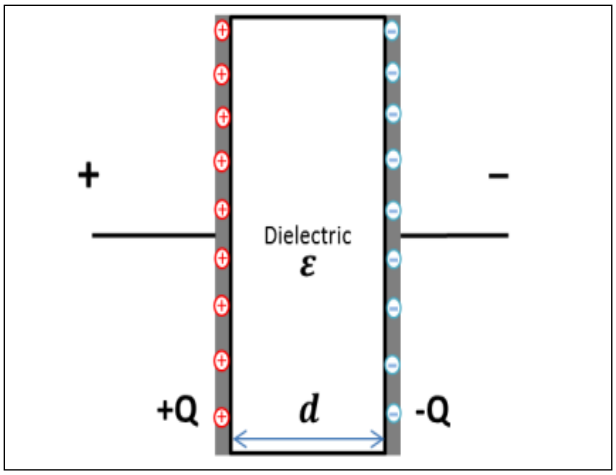

Figure 1.2: Schematic of an electrostatic capacitor

A key characteristic of a capacitor is its capacitance, which is defined as the ratio of the amount of electric charge (Q) stored on the electrodes to the voltage applied (V) across them. This parameter determines how much charge a capacitor can hold at a given voltage, given as:

$$\boldsymbol{C = \frac{Q}{V}}$$

To obtain high capacitance, several factors must be optimized. This includes selecting dielectric materials with a high permittivity, minimizing the distance between the electrodes, and—most crucially—developing innovative electrode materials that offer a significantly enhanced surface area [11].

When evaluating the performance of an energy storage device, two key parameters are considered: energy density (also referred to as specific energy) and power density (also known as specific power). These metrics represent the amount of energy or power delivered per unit mass of the device. The energy stored in a capacitor can be calculated using the equation:

$$\boldsymbol{E = \frac{1}{2} CV^2}$$

where E is the energy (in joules),

C is the capacitance (in farads), and

V is the voltage (in volts).

To determine a capacitor's power density, it's also important to consider the time it takes to discharge. Power density is typically calculated by dividing the stored energy by the discharge time, providing insight into how quickly the device can deliver its energy. Conventional capacitors typically exhibit extremely high-power density, often exceeding **5000 W/kg**, yet their energy density remains quite low, usually ranging between **0.01 and 0.05 Wh/kg**. Compared to batteries and fuel cells, capacitors have the advantage of being able to charge and discharge very quickly. However, this speed comes at the cost of limited energy storage capacity, making them less suitable for applications that require sustained energy delivery over longer periods.

1.1.3 Supercapacitors

Due to the inherently slow energy output of batteries and fuel cells, and the growing demand for rapid-response, high-power energy storage solutions, supercapacitors have emerged as a focal point of research and development. A generalized representation of a supercapacitor is illustrated in **Figure 1.3**. Structurally, supercapacitors resemble traditional capacitors, featuring a layered configuration composed of two electrodes with high porosity [12]. These electrodes are submerged in an electrolyte and are separated by an ion-permeable membrane. Upon the application of an external voltage, positive and negative charges accumulate on the respective surfaces of the electrodes. This causes ions within the electrolyte to migrate through the separator and penetrate the porous structure of the electrodes, driven by electrostatic forces. The design of the electrodes ensures that these ions remain separated, preventing charge recombination. As a result, an electric double layer forms at each electrode interface [12].

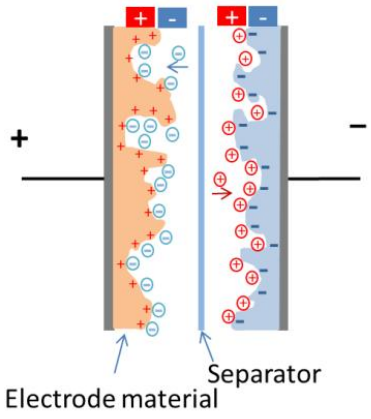

Figure 1.3: Schematic illustration of a supercapacitor

Supercapacitors operate on the same foundational concepts as traditional capacitors but distinguish themselves by incorporating electrodes with exceptionally large surface areas and a thin separator that acts as the dielectric medium. This configuration significantly enhances both their capacitance and energy storage capabilities. Moreover, thanks to their extremely low equivalent series resistance (ESR), comparable to that of standard capacitors, supercapacitors are capable of delivering exceptionally high-power output. To enhance the energy storage capacity and overall performance of supercapacitors, materials with extensive surface area and minimal spacing between electrodes are preferred. These characteristics enable greater charge accumulation and more efficient energy storage, aligning with the operational principles of supercapacitors [13].

1.2 Comparison between energy storage devices

The Ragone plot is a typical method to analyze the energy storage performance of any device [**Figure 1.4**]. The dashed lines on the chart represent the duration needed to either charge or discharge the device. From this illustration, it is evident that while traditional capacitors exhibit significantly higher power density than fuel cell batteries, they fall short in energy density, i.e., they store less energy. In contrast, while batteries and fuel cells can store larger amounts of energy, their performance under rapidly changing conditions is relatively limited. Supercapacitors, however, offer a balance between the two, they can deliver more power than a battery and store more energy than a typical capacitor. This means they are capable of extremely fast charging and discharging while still retaining a respectable amount of energy relative to their mass. As a result, they are particularly effective in applications requiring bursts of high power, such as regenerative braking systems, acceleration in electric vehicles, and uninterruptible power supplies.

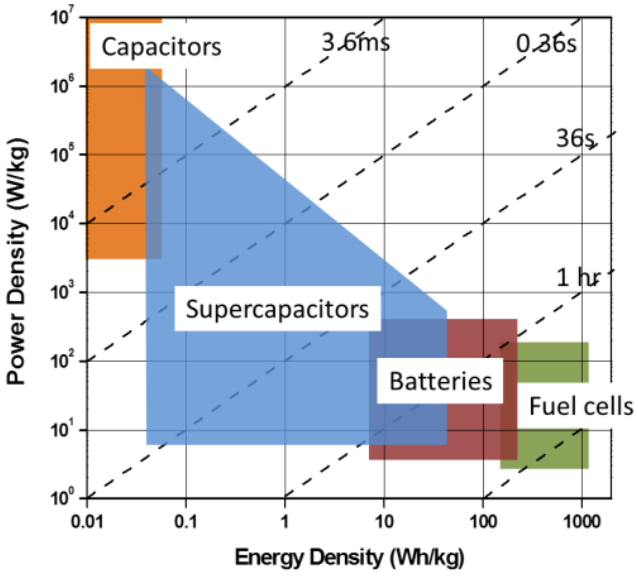

Figure 1.4: Ragone plot for various energy storage devices

The core reason for the existence of supercapacitors, despite having two very well-known energy storage devices, is the varied electrochemical stability and capabilities that it brings along with it. Beyond serving as a bridge between the high-power output of capacitors and the high-energy storage of batteries, supercapacitors bring several additional advantages that position them as strong contenders for future energy storage technologies. Since their energy storage mechanism is based on a purely physical process, without relying on chemical reactions or phase transformations, it is highly reversible. This allows them to undergo a vast number of charge-discharge cycles, often reaching up to a million repetitions. Furthermore, they function reliably across a broad range of temperatures.

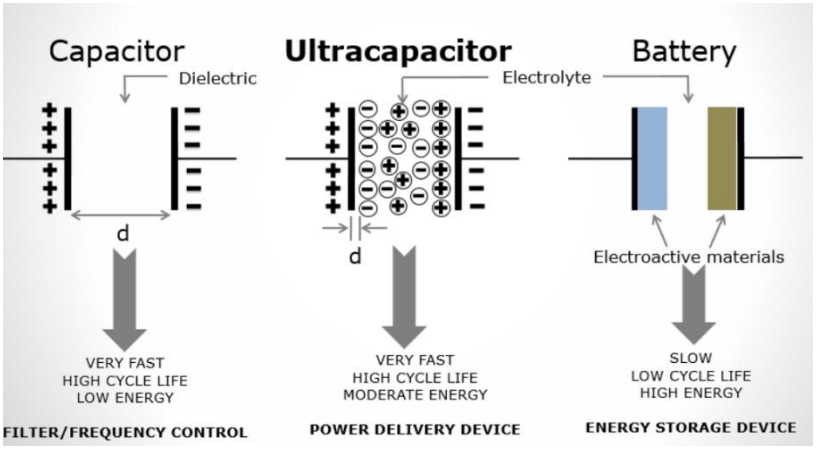

Figure 1.5: Current Energy Storage Systems: State of the Art

Table 1.1 outlines the comparative performance characteristics of these different devices. Despite notable strengths such as rapid charging and discharging, extended cycle life, lightweight design, high power output, and environmental safety, one major limitation to the widespread use of supercapacitors remains their cost. To enhance their performance, ongoing research focuses on developing advanced electrolytes that expand the operating voltage window, innovative dielectric materials with greater porosity, reduced thickness, and higher permittivity, as well as electrode materials with significantly larger surface areas [11].

Parameters	Capacitors	Batteries	Fuel cells	Supercapacitors
Charge/discharge time	1 ps-1 ms	1-10 hours	Not applicable	1 ms-1 s
Cycle life (cycles)	More than 1 million	150-2,000	Not applicable	Up to 1 million
Energy density (Wh/kg)	0.01-0.3	30-265	500-2,000	0.5-20
Power density (W/kg)	>5,000	100-3,000	1-1,000	5,000-10,000
Cost per Wh	0.10-1.00	1-2	0.035-0.05	10-20
Operating voltage range (V)	6-800	1.2-4.2	0.6-0.7	1.0-4.5
Operating temperature range (°C)	-20 to +100	-20 to +65	+50 to +1000	-40 to +85

Table 1.1: Comparison of capacitors, batteries, fuel cells, and supercapacitors

1.3 Types of supercapacitors and their working mechanism

Based on their energy storage mechanisms, supercapacitors are generally classified into three categories: electric double-layer capacitors (EDLCs), pseudocapacitors, and hybrid capacitors, as illustrated in **Figure 1.6**. EDLCs store energy through electrostatic accumulation within the Helmholtz double layer formed at the interface between the electrode and the electrolyte. These capacitors typically use carbon-based materials as electrodes, such as activated carbon, carbon aerogels, carbon nanotubes (CNTs), and, more

recently, graphene. In contrast, pseudocapacitors store energy via faradaic processes, specifically redox reactions involving charge transfer between the electrode and electrolyte. Common materials used in pseudocapacitor electrodes include conductive polymers, such as polyaniline, polypyrrole, and polythiophene, and various metal oxides, such as ruthenium oxide, manganese oxide, tin oxide, and cobalt oxide [4].

However, each type has its drawbacks: EDLCs tend to suffer from lower capacitance, while pseudocapacitors often face issues related to long-term stability. To address these limitations, hybrid supercapacitors have been developed. These combine carbon materials with pseudocapacitive components to leverage both storage mechanisms for improved performance. The primary distinguishing factor among these devices lies in the choice of electrode material.

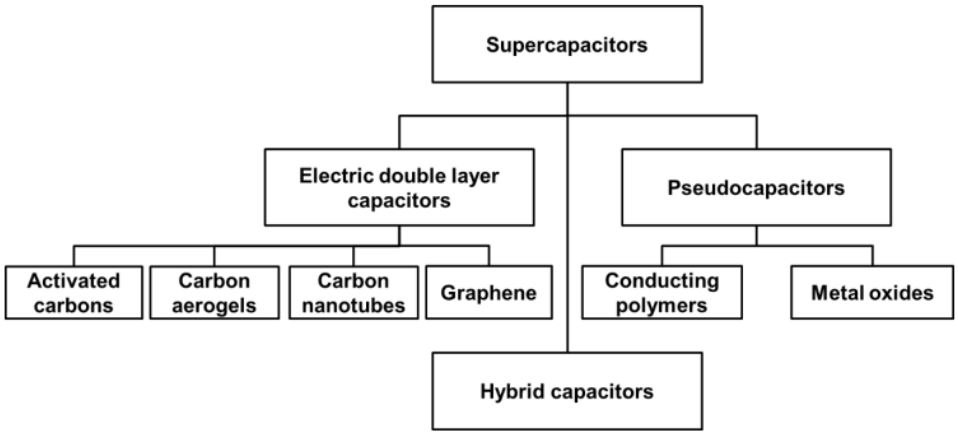

Figure 1.6: Classification of supercapacitors and related electrode materials

1.3.1 Electrochemical Double Layer Capacitors (EDLC)

Electric double-layer (EDL) capacitors store charge through the formation of an electric double layer at the interface between the electrode and electrolyte [**Figure 1.7**]. In practice, the nature of the solvent plays a critical role in ion solvation. Polar aprotic solvents, such as acetonitrile, are more effective at solvating cations, whereas polar protic solvents, including water and alcohols, are better at solvating anions. Since polar protic solvents are commonly used in supercapacitor electrolytes, cations tend to be well solvated, while anions are less so. According to the Helmholtz model, the EDL behaves like a basic capacitor, where two layers of opposite charges form across a small separation at the electrode-electrolyte interface. On a positively charged electrode surface, anions align

closely, creating a compact layer and a linear variation in electric potential across the interface. EDLC types of supercapacitors are mostly made up of carbonaceous materials and provide a larger surface area and store charge electrochemically [15].

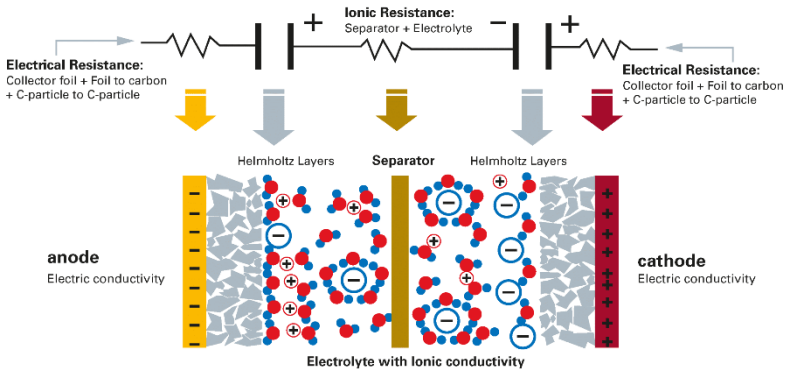

Figure 1.7: Electrochemical Double Layer Capacitor (EDLC)

1.3.2 Pseudocapacitors

Unlike electric double-layer (EDL) supercapacitors, pseudocapacitors store energy through faradaic processes that occur at the electrode–electrolyte interface. These processes typically involve mechanisms such as electrosorption, redox reactions, and ion intercalation. To enhance the specific capacitance of the electrodes, materials with inherent pseudocapacitive properties—such as conducting polymers and metal oxides—are employed either directly in pseudocapacitors or in combination with carbon-based materials to form hybrid supercapacitors.

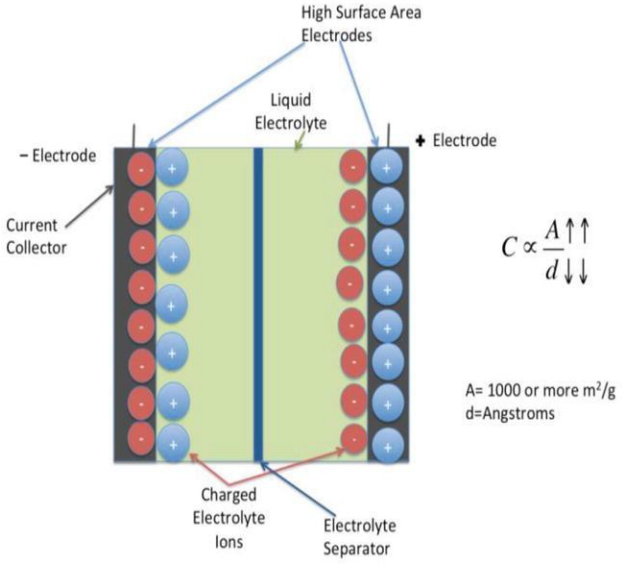

Figure 1.8: Pseudocapacitor

1.2.3 Hybrid Supercapacitor

Hybrid supercapacitors combine the benefits of electric double-layer capacitors and pseudocapacitors by integrating materials that support both electrostatic and faradaic charge storage [**Figure 1.9**]. Typically, these devices use a combination of carbon-based materials for high surface area and fast charge-discharge performance, along with metal oxides or conducting polymers to introduce redox activity and increase capacitance. This dual mechanism allows hybrid supercapacitors to achieve a better balance between energy density and power output, making them promising candidates for advanced energy storage applications.[9] These types of supercapacitors store charge both electrochemically and electrostatically, in a single system, and enhance the electrochemical stability of the device.[14]

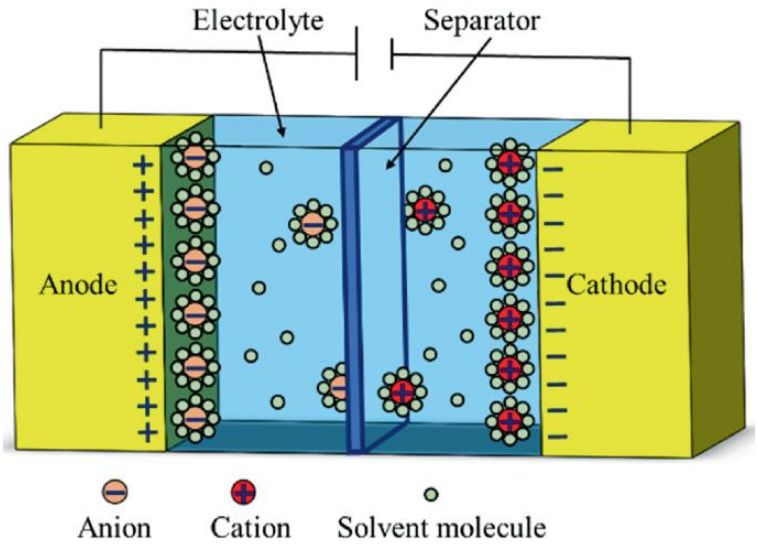

Figure 1.9: Hybrid-type supercapaitor

1.4 Polyoxometalates (POMs)

Polyoxometalates (POMs) are a class of metal-oxygen clusters composed primarily of early transition metals such as molybdenum, tungsten, and vanadium in their highest oxidation states. These clusters exhibit a rich diversity of structures, ranging from simple building blocks to intricate frameworks like the well-known Keggin and Dawson types [3] [1]. Their unique combination of structural versatility and tunable chemical properties has made

POMs an area of growing interest in fields such as catalysis, materials science, and biomedical research [3].

The synthesis of POMs is central to harnessing their functional potential. Typically carried out in aqueous solutions under carefully controlled pH and temperature conditions, their formation involves the self-assembly of metal-oxo units in the presence of heteroatoms such as phosphorus or silicon. Subtle variations in synthetic parameters, such as concentration, acidity, and reaction time, can significantly influence the final structure, size, and stability of the resulting polyoxo species. These are mainly formed by transition metals (M= Mo, W, V, and Nb) in their highest oxidation state with oxide ligands. Recent advances in synthetic methods have enabled the design of more complex POM architectures, including hybrid organic-inorganic structures and nanocomposites. These developments aim to improve solubility, enhance stability, and expand the range of applications.

1.3.1 Structural types in Polyoxometalates (POMs)

POMs are classified into two categories. First is isopolyanions and second is heteropolyanions. Isopolyanions are composed of only addenda atoms (M= Mo, V, W, and Nb) with oxygen ligands. Examples of isopolyanions are $[M_6O_{19}]^{2-}$, where the ion is composed of six edge-shared MO_6 octahedra. Heteropolyanions contain heteroatoms that may be from the main group or d-block elements. For example, $[SiW_{12}O_{40}]^{4-}$, $[PMo_{12}O_{40}]^{3-}$ are called Keggin ions. Keggin ions are composed of a central tetrahedral XO4 hetero group surrounded by 12 MO_6 (M = Mo, W) octahedral units. An example of another heteropolyanion is the Well-Dawson species, for example $[P_2W_{18}O_{62}]^{6-}$, which consists of two XO_4 heterogroups and 18 addenda atoms [2].

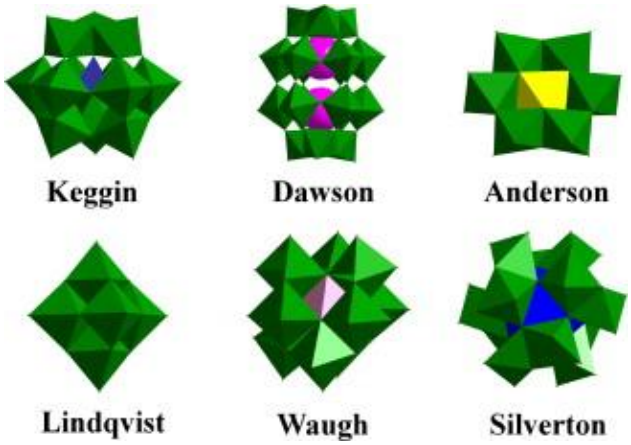

Figure 1.10: Polyhedral representation of some common isopolyanions and heteropolyanions

1.3.2 Synthesis Strategies

Heteropolyanions and isopolyanions are generally formed and isolated from aqueous solution. POMs synthesis is simple, involves few steps, or just one step (one-pot synthesis). In a typical "one-pot" synthesis method, acidification of precursor metal ions, such as sodium tungstate, is carried out in aqueous solution in the presence or absence of heteroelements. Acidic medium allows the linking of polyhedral units $\{MO_x\}$ (where M is Mo, W; x = 4-7), by corner and edge sharing, then self-assemble to form various polyanions depending on the reaction conditions, like pH, temperature, and concentration of material. Now, the next step is the isolation of the polyanion. It is carried out by counter ions like alkali metal, organic cations like TBA, etc., and the precipitate was collected by a simple filtration process [16].

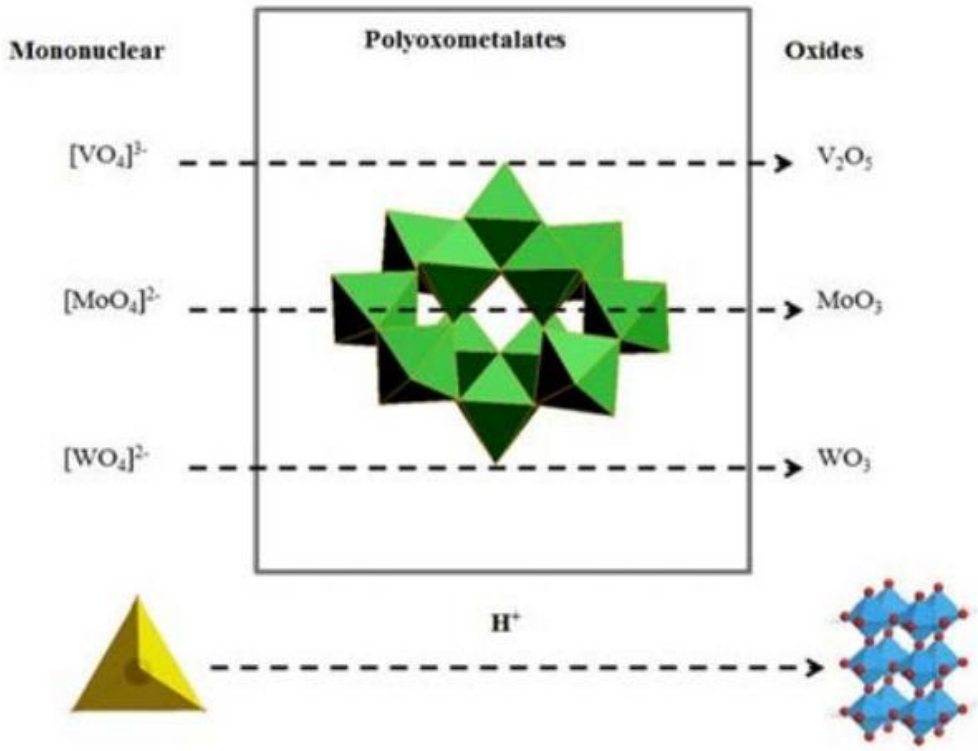

Figure 1.11: Scheme highlighting the fact that discrete POMs are in between $[MO_4]^{n-}$ and mono-extended solid oxides. The controlled acidification of a solution of $[MO_4]^{n-}$ leads to the formation of discrete structure POMs

Polyoxometalates (POMs) retain their solid-state structures even when dissolved in water. In cases where a particular POM is not water-soluble, its counter ions can be exchanged with more compatible ions to enhance solubility in aqueous media. The detailed structural information of POMs is typically obtained through single-crystal X-ray diffraction analysis. Given their stability at room temperature, these compounds can be stored for extended periods without degradation, allowing for their use in future applications.

1.3.3 Formation of Polyoxotungstates and Polyoxomolybdates

Under the particular conditions (e.g., pH, temperature, concentration), oxometalate ions get protonated to give rise to polycondensation of $\{MO_4\}^{3-}$ units and resulting in the formation of more complex structures known as polyanions. If the condensation takes place between similar species, polyanions with the general formula $\{M_nO_{(4n-m)}\}^{(2n-m)-}$ are formed.

$$\mathbf{nMO_4^{3-} + 2mH^+ \leftrightarrow M_nO_{(4n-m)}^{(2n-m)-} + mH_2O}$$

The formation of polyanions is generally kinetically controlled rather than thermodynamically.

1.5 Utility of POMs in the development of supercapacitors

Hybrid Vanado-Tungstate/Molybdate electrodes are preferred for Electrochemical applications due to the following reasons

i. Enhanced Electrochemical Performance: Synergistic effects from combining pseudocapacitive vanadium's redox activity with the double layer capacitance of carbonaceous materials.
ii. Improved Pseudocapacitance: Higher energy density is achieved through enhanced pseudocapacitive behavior compared to molybdenum or tungsten hybrids.
iii. Better Stability and Cycling Performance: Superior cycling stability and capacitance retention over extended charge-discharge cycles.
iv. Versatile Fabrication Techniques: Various processing methods (e.g., layer-by-layer deposition) allow for controlled morphology and functionality.

1.6 Perspective of current work

The current research project aims to understand the significance of vanadium in electrochemical energy storage processes. Vanadium, with its multiple stable oxidation states and flexible coordination environments, is an extremely versatile element for redox applications. Incorporation of vanadium into tungstates and molybdates, to form mixed hybrid poly-oxo-vanado-tungstate and molybdate derivatives, is expected to show enhancement in the charge storage properties of such polyoxometalate compounds, as these will increase the rate of electron transfer and the intercalation process for effective energy storage and power capacitive performance. Based on such a premise, we aim to prepare efficient electrode materials for the development of energy storage devices. These compounds also tend to increase the stability of the device. The synthesized materials and electrodes have been extensively characterization using FTIR, PXRD, and UV-VIS spectroscopy. Electrochemical analysis on prepared electrodes has been performed using cyclic voltammetry (CV), galvanostatic charge discharge (GCD) studies, and electrochemical impedance spectroscopy (EIS) techniques.

References

[1] D. M. Andoshe, J.-M. Jeon, S. Y. Kim and H. W. Jang. Two-dimensional transition metal dichalcogenide nanomaterials for solar water splitting. Electronic Materials Letters, 2015, 11, 323-335..

[2] A. Hiskia, A. Mylonas, E. Papaconstantinou. Comparison of the photoredox properties of polyoxometallates and semiconducting particles. Chemical Society Reviews, 2000, 30, 62–69..

[3] Y. Zhang, J. Liu, S. -L. Li, Z. -M. Su, Y. -Q. Lan. Polyoxometalate-based materials for sustainable and clean energy conversion and storage. EnergyChem, 2019, 1, 100021..

[4] G. Wang, L. Zhang and J. Zhang, A review of electrode materials for electrochemical supercapacitors, Chem. Soc. Rev., 41, pp. 797-828, 2012..

[5] M. Armand and J. M. Tarascon, Building better batteries, Nature, 451, 652- 657, 2008..

[6] C. Liu, Z. Yu, D. Neff, A. Zhamu, and B. Z. Jang, Graphene-based supercapacitor with an ultrahigh energy density, Nano Lett., 10, 4863-4868, 2010..

[7] M. Ammam. Polyoxometalates: formation, structures, principal properties, main deposition methods and application in sensing, Journal of Materials Chemistry A, 2013, 1 (21), 6291-6312..

[8] S. Knoth, 2-A supercap charger balances and protects cells in portable applications, Power-eetimes, 222901984, 2010..

[9] A. Dupuis, Proton exchange membranes for fuel cells operated at medium temperatures: Materials and experimental techniques, Progress in Materials Science, 56, 289-327, 2011..

[10] M.T. Pope, Heteroply and Isopoly Oxometalates, Springer, Berlin, 1983..

[11] Mahala, S.; Khosravinia, K.; Kiani, A., Unwanted degradation in pseudocapacitors: Challenges and opportunities. J. Energy Storage 2023, 67, 107558..

[12] Si, H.; Seidl, L.; Chu, E. M. L.; Martens, S.; Ma, J.; Qiu, X.; Stimming, U.; Schneider, O., Impact of the morphology of V2O5 electrodes on the electrochemical Na+ -ion intercalation. J. Electrochem. Soc. 2018, 165 (11), A2709..

[13] Sankapal, B. R.; Gajare, H. B.; Karade, S. S.; Dubal, D. P., Anchoring cobalt oxide nanoparticles on to the surface multiwalled carbon nanotubes for improved supercapacitive performances. RSC Adv. 2015, 5 (60), 48426-48432..

[14] Morla, K. S.; Thakre, D.; Deshmukh, T. B.; Malo, S.; Ahamed, S.; Aparna, R. K.; Sahoo, S.; Sarma, D.; Mondal, K. C.; Sankapal, B. R.; Banerjee, A., In-depth understanding of electrochemical energy storage efficiency in a series of new 3d–4d mixed meta.

[15] S. Knoth, 2-A supercap charger balances and protects cells in portable applications, Power-eetimes, 222901984, 2010..

CHAPTER 2:

SYNTHESIS, CHARACTERIZATION AND METHODOLOGIES

2. SYNTHESIS, STRUCTURE, AND CHARACTERIZATION

All four compounds were prepared as per the literature procedures.

2.1 Synthesis

2.1.1 Phosphotungstic acid: $H_3[PW_{12}O_{40}]$

To 1.076 g (3.66 mmol) of Na_2WO_4, taken in a 50 ml beaker, 15 ml of water was added. The mixture was left for complete dissolution of Na_2WO_4 in the water. Further, HCl of molarity 12M was added until the pH of the mixture reached 1-2. Once the pH between 1-2 was attained, the mixture was kept for heating at 50 °C for 2 minutes. Further 16 µL of Phosphoric acid was added to the solution to maintain a pH of 1.89. The addition was Phosphoric acid was done at 80 °C. The solution was then kept for stirring with constant heating at 80 °C for 3h. A white crystalline product was obtained by filtration and washed with Methanol.

$$Na_2WO_4 \xrightarrow[pH= 1.89,\ Water]{HCl,\ H_3PO_4} H_3[PW_{12}O_{40}]$$

Scheme 2.1: Synthesis of Phosphotungstic acid

2.1.2 Phosphomolybdic acid: $H_3[PMo_{12}O_{40}]$

To 1.44 g (10 mmol) of MoO_3, taken in a 50 ml of beaker, 15 ml of water was added. To the mixture, 5.6 ml (96 mmol) of Phosphoric acid was added. Th resultant mixture was put to boil for 30 minutes. Then further to resultant mixture started to develop some light green colour, it was put on heating for 90 °C for 3 h with constant stirring. The green colour developed during heating was removed using bromine water which resulted in a yellow colour solution. This solution was cooled down and put again to concentrate to half the volume. On cooling the solution, light yellow-green colour of crystals were obtained. The product was obtained by filtration.

$$MoO_3 \xrightarrow[Water]{H_3PO_4} H_3[PMo_{12}O_{40}]$$

Scheme 2.2: Synthesis of Phosphomolybdic acid

2.1.3 Vanado-Tungstate derivative: $(NH_4)_6H[PV_4W_8O_{40}]$

0.49 g (4.091 mmol) of $NaVO_3$ was added to 2.5 ml of water in a 20 ml beaker, and the resultant mixture was on stirring for 20 minutes. In another 20 ml of beaker, 2.2 g (6.66 mmol) of Na_2WO_4 was added to 2.5 ml of hot water, and the resultant solution was put on stirring for 20 minutes. The two solutions were mixed together, and on mixing a yellow colour solution was observed. The yellow colour solution was put to stirring for 30 minutes to form a homogenous solution. The resultant solution was cooled to room temperature. Once the solution attained room temperature, 0.5 ml of Phosphoric acid was added to it. The solution then turned dark red. The dark red solution was then put to heat with constant stirring at 95 °C for 1 h. During this time, the solution changed its colour from dark red to orange-red. Once the solution was cooled to room temperature, 0.35 g (6.54 mmol) of NH_4Cl was added to the resulting solution, post which, the precipitation began and orange-red crystals of the compound were obtained on filtration.

$$NaVO_3 + Na_2WO_4 + H_3PO_4 \xrightarrow{NH_4Cl,\ H_2O,\ 95^oC,\ 1h} (NH_4)_6H[PV_4W_8O_{40}]$$

Scheme 2.3: Synthesis of $(NH_4)_6H[PV_4W_8O_{40}]$

2.1.4 Vanado-Molybdate derivative: $H_6[PV_3Mo_9O_{40}]$

0.53 g (3.7 mmol) of MoO_3 was added to 30 ml of water in a 50 ml of beaker and stirred until completely dissolved. Stoichiometric amount of 0.0305 g (0.1682 mmol) of V_2O_5 was added to the above solution. The resultant mixture was then heated to boil, followed by 20 µL (0.3364 mmol) of Phosphoric acid. The resultant mixture was refluxed for 6h, allowing the reaction to complete. After cooling to room temperature, a clear solution was obtained. The solvent was then evaporated, yielding a solid acid compound which was further purified through recrystallization, thereby, obtaining the compound.

$$MoO_3 + V_2O_5 + H_3PO_4 \xrightarrow{H_2O,\ reflux,\ 6h} H_6[PV_3Mo_9O_{40}]$$

Scheme 2.4: Synthesis of $H_6[PV_3Mo_9O_{40}]$

2.2 Characterization Techniques

2.2.1 Powder X-ray diffraction (P-XRD)

P-XRD analytical technique was used towards determining the phase purity and confirming the crystalline behaviour of the synthesised compounds. P-XRD data were collected on Bruker D8ECO with Cu Kα source radiation (Cu, λ = 1.54056 Å) from an angular range 5 - 60° in a 2θ scale, at 298 K.

2.2.2 Fourier transform infrared (FT-IR) spectroscopy

Infrared spectra were recorded on a ThermoFisher Scientific Nicolet iS50 FT-IR spectrophotometer, and prepared KBr pellets for the measurement (4000 – 400 cm^{-1}). The following abbreviations were used to assign peak intensities: w: weak; m: medium; s: strong; vs: very strong, and b: broad. Fourier transformed infrared (FTIR) spectra were acquired using a Bruker 4000 (USA) spectrometer in the wavenumber range of 4000 – 400 cm^{-1}.

2.2.3 Optical Spectroscopy

- **Solution-phase:** UV-vis spectra of aqueous solutions of synthesised compounds were measured on a double-beam spectrophotometer, JASCO UV (V-630)**,** in the range of 190−1100 nm. For the time-dependent UV−vis spectra, the aqueous solution of the compound(s) was kept standing in the cuvette and spectra were measured at periodic time intervals**.**
- **Solid Phase:** UV-vis spectra of aqueous solutions of synthesised compounds were measured on Shimadzu UV-2600, in the range of 200−800 nm. For the time-dependent UV−vis spectra, the aqueous solution of the compound(s) was kept standing in the cuvette and spectra were measured at periodic time intervals.

2.3 Fabrication of Electrodes by Doctor Blade Technique

Crafting electrodes with the doctor blade method provides more precise and functional outcomes. It is an essential methodology in electrode fabrication due to its unique versatility and scalability. The importance of this technique lies in its ability to produce uniform thin films of electrode materials over a substrate with relative ease and effectiveness. This uniformity is paramount for ensuring consistent performance across the electrode surface, directly impacting the efficiency of the electrochemical device it will be

a part of. Furthermore, this technique is adaptable to various substrate materials and geometries. The thickness of the deposited films can be precisely controlled by adjusting the gap height of the doctor blade, offering tunability for various applications.

A thin slurry of the electrode material- perhaps a blend of conductive powders and binders is carefully spread across a substrate (Eg, Stainless steel, CNT, etc.) using a very fine, straight-edged blade. As the blade glides, it leaves behind a uniform film of the desired thickness. This seemingly allows for the creation of consistent and controlled electrode layers. After drying and some heat treatment, this delicate film transforms into a robust electrode, ready to play its part in energy storage, sensing and catalysis. The pictorial representation of the development of electrodes using doctor blade method is presented below.

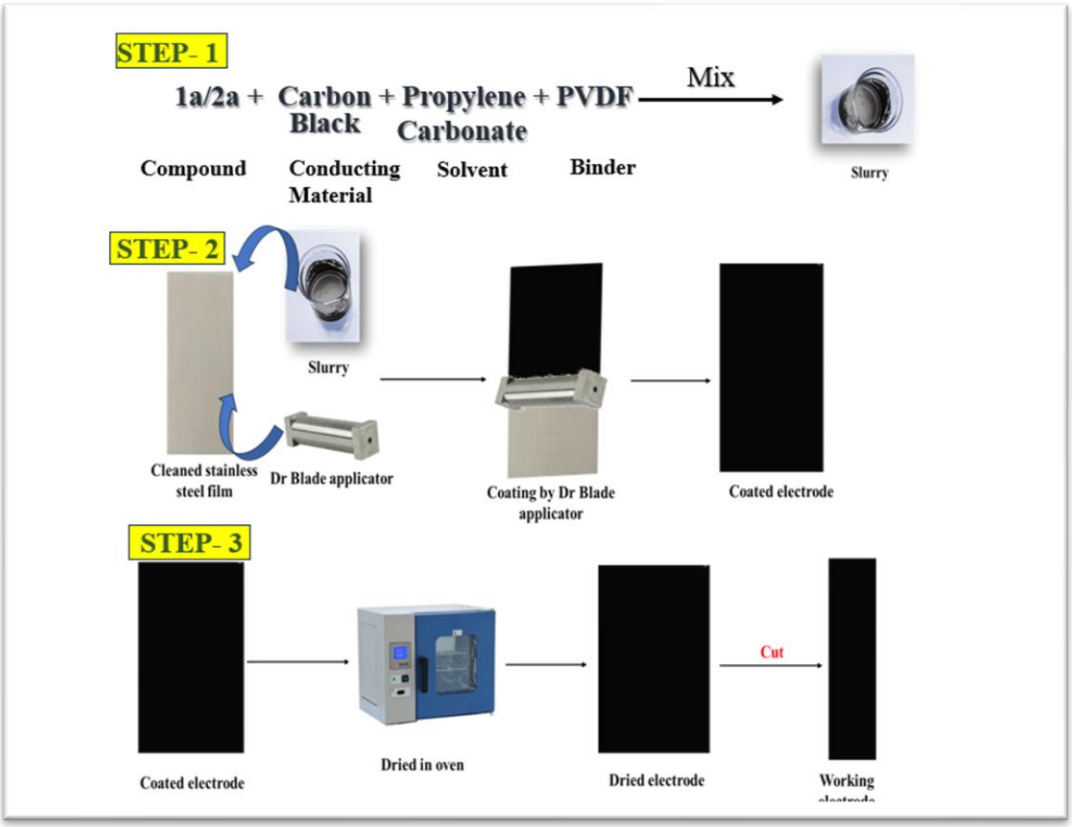

Figure 2.1: Fabrication of electrode

2.4 Electrochemical Studies: Supercapacitive Properties

The electrochemical studies were performed using a PARSTAT 4000 potentiostat/galvanostat (Princeton Applied Research, USA) electrochemical workstation, in a three-electrode cell assembly where we used:

- Working Electrode: Stainless steel coated electrode
- Counter Electrode: Platinum Electrode
- Reference Electrode: Ag/AgCl Electrode
- Electrolyte and solvent Used: 1M $LiClO_4$ with Propylene Carbonate and Ethylene Carbonate.

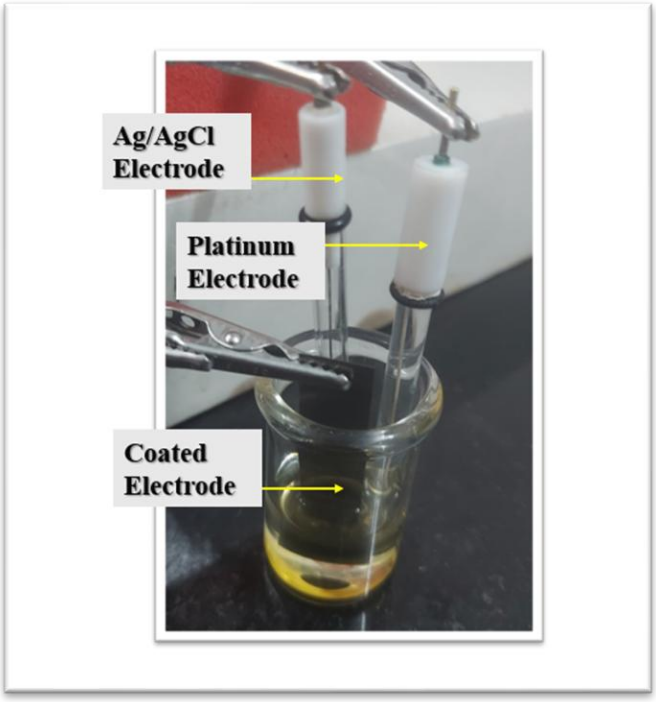

Figure 2.2: Three-electrode system

The electrochemical studies performed using this three-electrode system were as follows:

2.4.1 Cyclic Voltammetry

CV analysis was performed at room temperature

For calculation of areal capacitance from the CV data we used the formula:

$$C = \frac{\int Idv}{(v * \Delta V * A)}$$

Where, C = areal capacitance (F/cm^2)

$\int Idv$ represents the integral of the current (I) with respect to voltage (V) across the potential window

v is the scan rate in V/s

ΔV is the potential window, and A is the area of the electrode, 1 cm^2

2.4.2 Galvanostatic Charge Discharge

Using the formula, we can calculate the areal capacitance of the compound

$$\boldsymbol{C = \frac{2 * I * t}{V * A}}$$

where, I = Current

t= Discharge time

V= Potential Window, and

A= Area of cross section

2.4.3 Electrochemical Impedance Spectroscopy

EIS analysis was performed to determine solvent and charge transfer resistance properties within the electrochemical cell using our as prepared electrodes.

CHAPTER 3: RESULTS AND DISCUSSION

3. Results and Discussion

In this research project, we have aimed to explore the effect of vanadium incorporation into oxotungstates and oxomolybdates on their electrochemical properties. This Chapter presents the results obtained by performing various methodologies mentioned in chapter 2. The vanadium-containing derivatives showed enhanced capacitance, ostensibly due to vanadium's excellent redox properties, and ability to exist in different oxidation states and stable geometries; which accounts for better electron transfer and stability of the synthesized compounds.

3.1 Structure of synthesized compounds

All four synthesized compounds have isostructural Keggin-type assembly, composed of 12 $\{MO_6\}$ octahedral coordination polyhedra and one tetrahedrally coordinated PO_4 group [**Figure 3.1**]. As part of this research work, we have substituted some tungsten and molybdenum atoms, in oxo-tungstates and oxo-vanadates, respectively, with vanadium atoms.

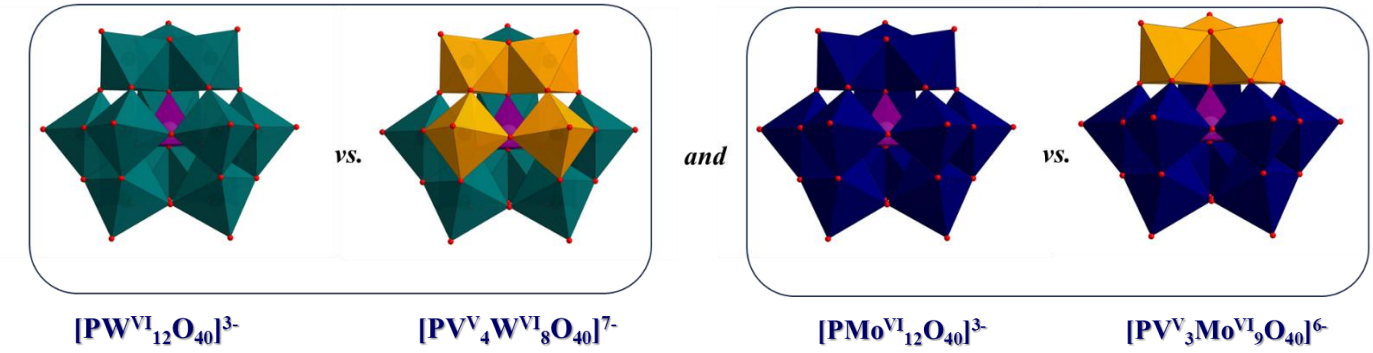

Figure 3.1: Polyhedral representation of $[PW_{12}O_{40}]^{3-}$ *vs.* $[PV_4W_8O_{40}]^{7-}$, and $[PMo_{12}O_{40}]3-$ *vs.* $[PV_3Mo_9O_{40}]^{6-}$. Color code: Green polyhedra – $\{WO_6\}$, Dark blue polyhedra – $\{MoO_6\}$, Orange polyhedra – $\{VO_6\}$, Magenta polyhedral – $\{PO_4\}$.

3.2 Characterization of synthesized compounds

3.2.1 Powder X-ray Diffraction

The powder X-ray diffraction (PXRD) method was employed towards determining the crystallinity of the synthesized compounds. The sharp peaks in the pattern confirm the crystalline characteristic of the materials for all four synthesized compounds, namely,

$H_3[PMo_{12}O_{40}]$, $H_3[PW_{12}O_{40}]$, and their vandate derivatives $H_6[PV_3Mo_9O_{40}]$ and vanado-tungstate $(NH_4)_6H[PV_4W_8O_{40}]$.

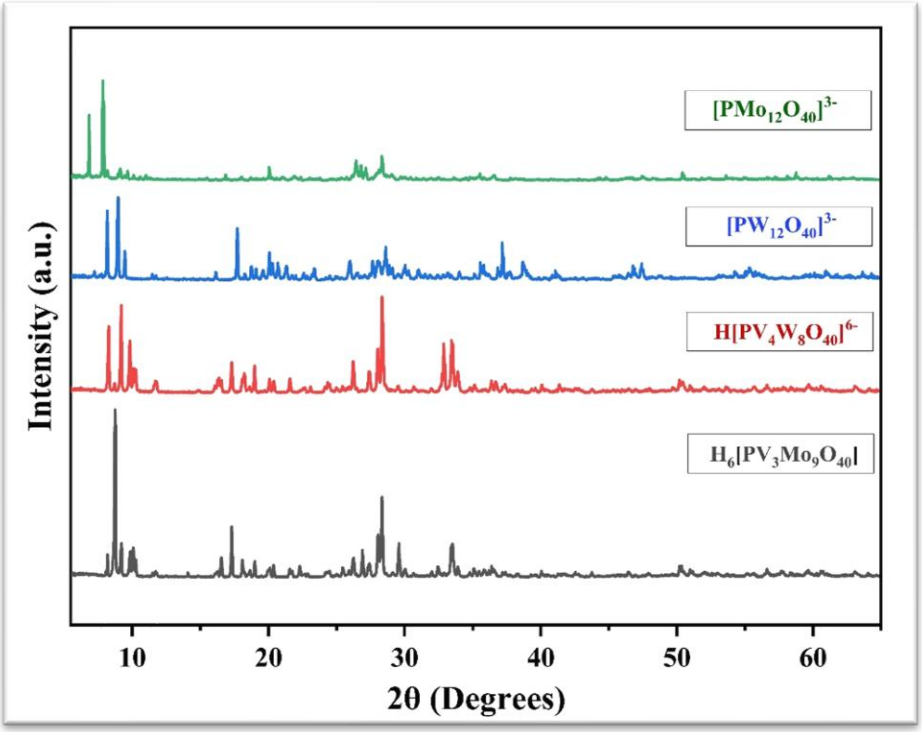

Figure 3.2: PXRD Data of the synthesized materials

3.2.2 Infrared Spectroscopic Studies

All four synthesized compounds are isostructural. Infrared spectroscopic studies were used to confirm the formation of the Keggin unit is all four polyanionic assemblies. We have tried to assign vibrational peaks observed in the infrared spectra for compounds based on literature references of vanadium oxo complexes and phosphate groups. The broad vibrational peak at ~3400 cm^{-1} and the sharp peak at ~1600 cm^{-1} are characteristic of stretching vibration of (O-H) and bending vibration of (O-H) in the lattice, while the sharp peak at 1400 cm^{-1} can be ascribed for the H-N-H stretching from the ammonium counterions for $(NH_4)_6H[PV_4W_8O_{40}]$.

For all four compounds, the strong vibrational peaks at 1168 and 1061 cm^{-1} can be associated with P-O stretching. For $(NH_4)_6H[PV_4W_8O_{40}]$ and $H_6[PV_3Mo_9O_{40}]$, the strong stretching vibrational peak(s) in the region 955-930 cm^{-1} can be attributed to V=O stretching, and peaks at ~820 cm^{-1} is attributed to the O-V-O vibration for, which suggests

the incorporation of V into the structures. For $(NH_4)_6H[PV_4W_8O_{40}]$, and $H_3[PW_{12}O_{40}]$, peaks in the region 580 – 500 cm^{-1} are assigned to W-O stretching. Whereas for $H_3[PMo_{12}O_{40}]$ and $H_6[PV_3Mo_9O_{40}]$, Peaks in the region 650 – 500 cm^{-1} are assigned to Mo-O stretching.

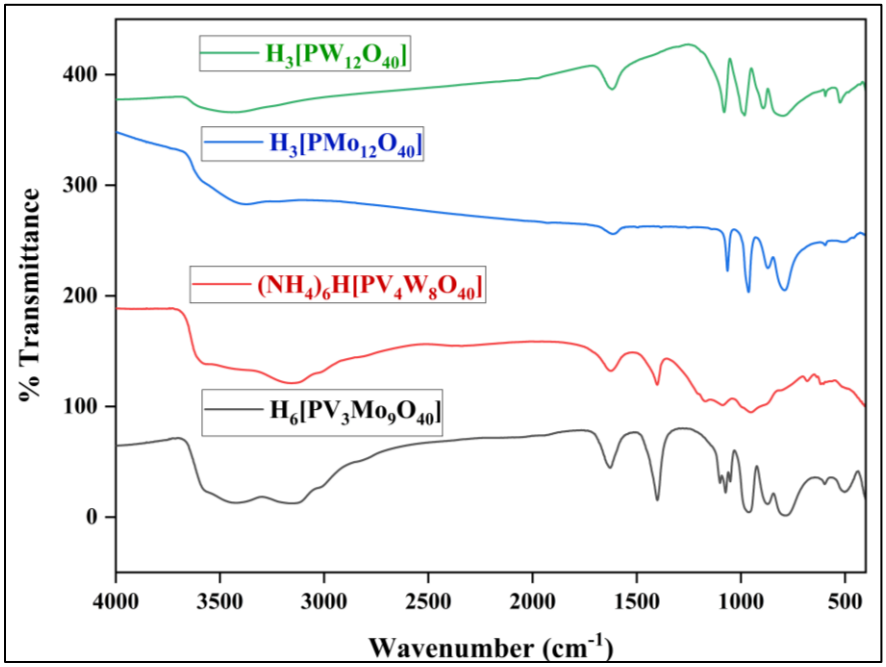

Figure 3.3: Infrared Spectra

3.2.3 UV-Visible spectroscopy

(a) UV-Visible data for $H_3[PW_{12}O_{40}]$, and $(NH_4)_6H[PV_4W_8O_{40}]$

UV-Visible spectra for compounds $H_3[PW_{12}O_{40}]$ and $(NH_4)_6H[PV_4W_8O_{40}]$ was monitored in the range of 200 − 800 nm in aqueous solution. To check the stability of the synthesized compounds in the solution state, systematic studies of time-dependent UV-Visible spectra were monitored. $H_3[PW_{12}O_{40}]$ exhibited a strong absorption peak at 250 nm, attributed to the ligand to metal charge transition pπ-dπ (LMCT) transition from terminal oxygen atom to tungsten(VI), while another characteristic sharp absorption peak of $(NH_4)_6H[PV_4W_8O_{40}]$ at 249 nm is attributed to charge transfer pπ-dπ transition (LMCT) of from bridging oxygen (O_t) atom to Tungsten (VI) [**Figure 3.4(a)**].

The compound $(NH_4)_6H[PV_4W_8O_{40}]$ exhibited a strong shoulder peak at 360 nm in the spectra due to the insertion of vanadium into the $H_3[PW_{12}O_{40}]$ framework [**Figure 3.4(b)**].

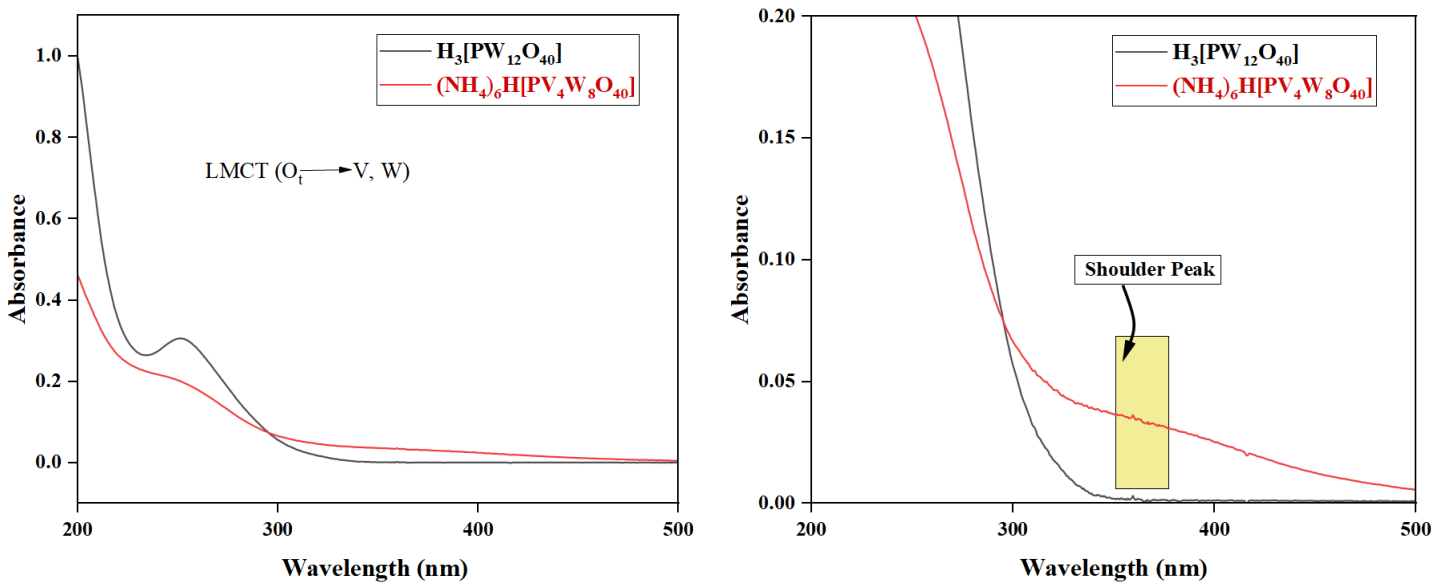

(a) **(b)**

Figure 3.4: UV-Visible spectra of $H_3[PW_{12}O_{40}]$, and $(NH_4)_6H[PV_4W_8O_{40}]$

(b) UV-Visible data for $H_3[PMo_{12}O_{40}]$, and $H_6[PV_3Mo_9O_{40}]$

UV-Visible spectra for compounds $H_3[PMo_{12}O_{40}]$ and $(NH_4)_6H[PV_4W_8O_{40}]$ was monitored in the range of 200 − 800 nm in aqueous solution. To check the stability of the synthesized compounds in the solution state, systematic studies of time-dependent UV-Visible spectra were monitored. $H_3[PMo_{12}O_{40}]$ exhibits a strong absorption peak at 212 nm, attributed to the ligand to metal charge transition pπ-dπ (LMCT) transition from terminal oxygen atom to Molybdnum(V), while another characteristic sharp absorption peak of at 257 nm is attributed to $H_6[PV_3Mo_9O_{40}]$ charge transfer pπ-dπ transition (LMCT) of from bridging oxygen (O_t) atom to Molybdnum (VI) [**Figure 3.5(a)**]. The compound $H_6[PV_3Mo_9O_4]$ exhibits a strong shoulder peak at 362 nm in the spectra due to the insertion of vanadium into the $H_3[PMo_{12}O_{40}]$ framework [**Figure 3.5(b)**].

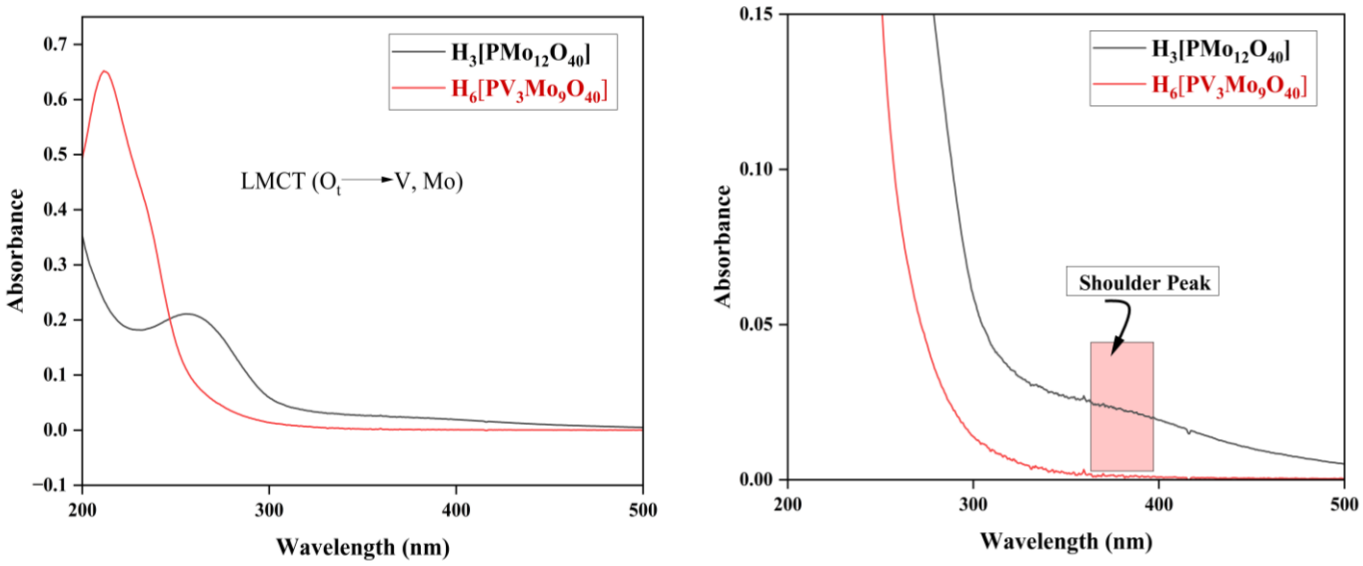

(a) **(b)**

Figure 3.5: UV-Visible spectra of $H_3[PMo_{12}O_{40}]$, and $H_6[PV_3Mo_9O_{40}]$

3.3 Electrochemical Studies

Electrochemical studies were performed to determine important parameters such as specific capacitance, energy and power density values.

3.3.1 Cyclic Voltammetry

Cyclic voltammetry measures the charge response of the electrode with increasing current density and scan rate, respectively. Here the potential is applied between the working electrode and the reference electrode and the current is calculated between the counter electrode and the working electrode. Specific areal capacitance values were calculated using the formula;

$$C = \frac{\int Idv}{(v * \Delta V * A)}$$

a) $(NH_4)_6H[PV_4W_8O_{40}]$

The quasi-rectangular nature if the cyclic voltammetry suggests supercapacitive nature of the compound [**Figure 3.6**]. The redox peaks are not clearly visible in the curve due to the intercalation process occurring in the compound. Here we can observe that the current density increases with increasing scan rate

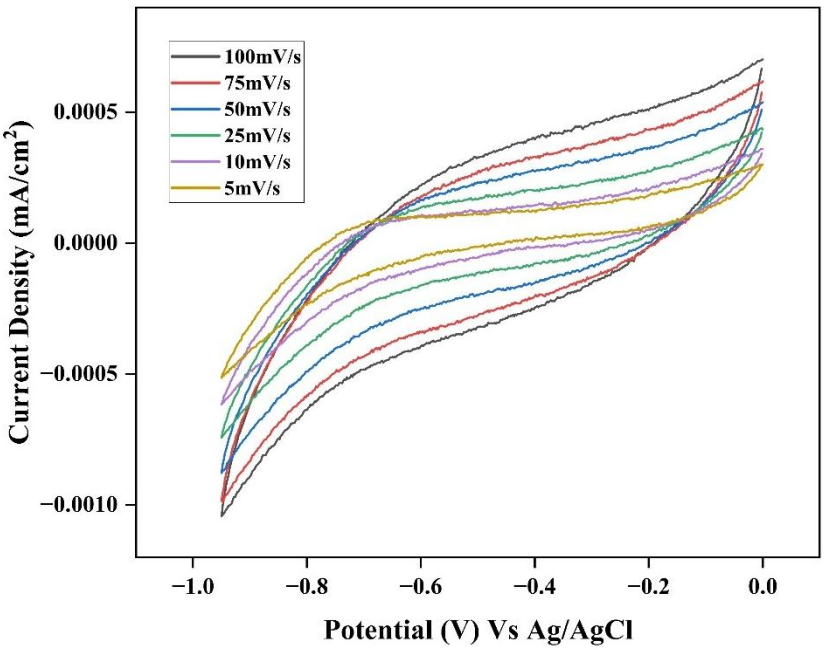

Figure 3.6: CV Curve for $(NH_4)_6H[PV_4W_8O_{40}]$

The highest areal capacitance was calculated as 56.88 mF/cm^2 at 5 V/s scan rate, respectively, as presented in the **Table 3.1** presented below.

Table 3.1: Areal capacitance values for $(NH_4)_6H[PV_4W_8O_{40}]$

Scan Rate (mV/s)	Voltage Window (V)	Area (cm^2)	C (F/cm^2)	C (mF/cm^2)
100	0.95	7.37 x 10^{-4}	0.007754	7.753733
75	0.95	6.49 x 10^{-4}	0.009112	9.112481
50	0.95	5.47 x 10^{-4}	0.011507	11.50725
25	0.95	4.25 x 10^{-4}	0.017913	17.9133
10	0.95	3.22 x 10^{-4}	3.39E-02	33.90302
5	0.95	2.70 x 10^{-4}	0.056881	56.88072

b) $H_6[PV_3Mo_9O_{40}]$

Similar to earlier case, the quasi-rectangular nature if the cyclic voltammetry suggests supercapacitive nature of the compound [**Figure 3.7**]. Here we can observe that the current density increases with increasing scan rate.

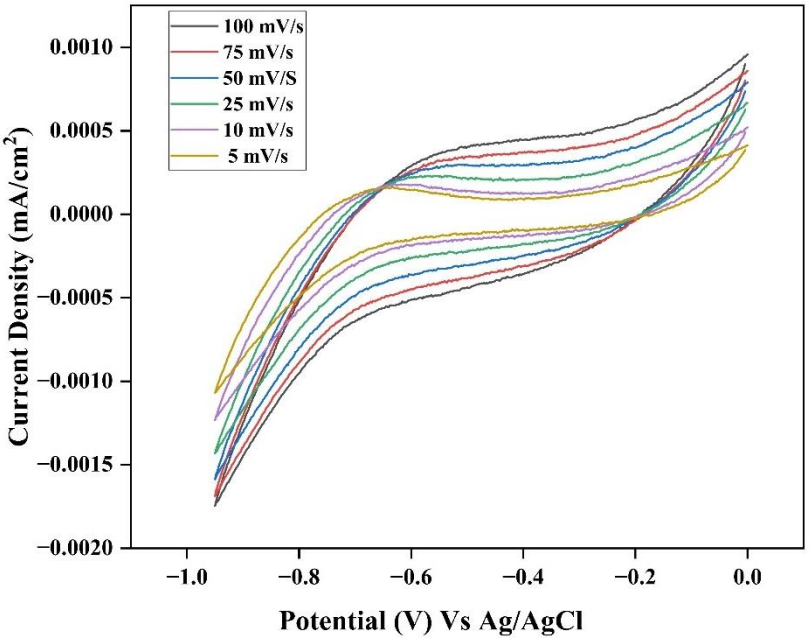

Figure 3.7: CV Curve for $H_6[PV_3Mo_9O_{40}]$

The highest areal capacitance is calculated as 51.79 mF/cm^2 at 5 V/s scan rate, respectively, as presented in the Table 3.3.1.b presented below.

Table 3.2: Areal capacitance values for $H_6[PV_3Mo_9O_{40}]$

Scan Rate (mV/s)	Voltage Window (V)	Area (cm^2)	C (F/cm^2)	C (mF/cm^2)
100	0.95	7.27 x 10^{-4}	0.007648	7.64847
75	0.95	6.89 x 10^{-4}	0.009674	9.673884
50	0.95	5.95 x 10^{-4}	0.012517	12.51694
25	0.95	4.54 x 10^{-4}	0.019133	19.13305
10	0.95	2.31 x 10^{-4}	2.43E-02	24.33767
5	0.95	2.46 x 10^{-4}	0.051793	51.79333

c) Comparison between $(NH_4)_6H[PV_4W_8O_{40}]$ and $H_3[PW_{12}O_{40}]$

The comparative cyclic voltammogram curve suggests the pseudocapacitive behavior for both the compounds, but we can observe that $(NH_4)_6H[PV_4W_8O_{40}]$ to show better areal capacitance in comparison with $H_3[PW_{12}O_{40}]$ [**Figure 3.8**]. This can be attributed to the incorporation of vanadium atom into the structure which thereby enhances the redox

activity of the compound. From the area under the curve, it is observed that at 100mV/s, $(NH_4)_6H[PV_4W_8O_{40}]^{6-}$ has a better areal capacitance of 7.75 mF/cm^2 in comparison to $H_3[PW_{12}O_{40}]$, which has an areal capacitance of 6.89 mF/cm^2.

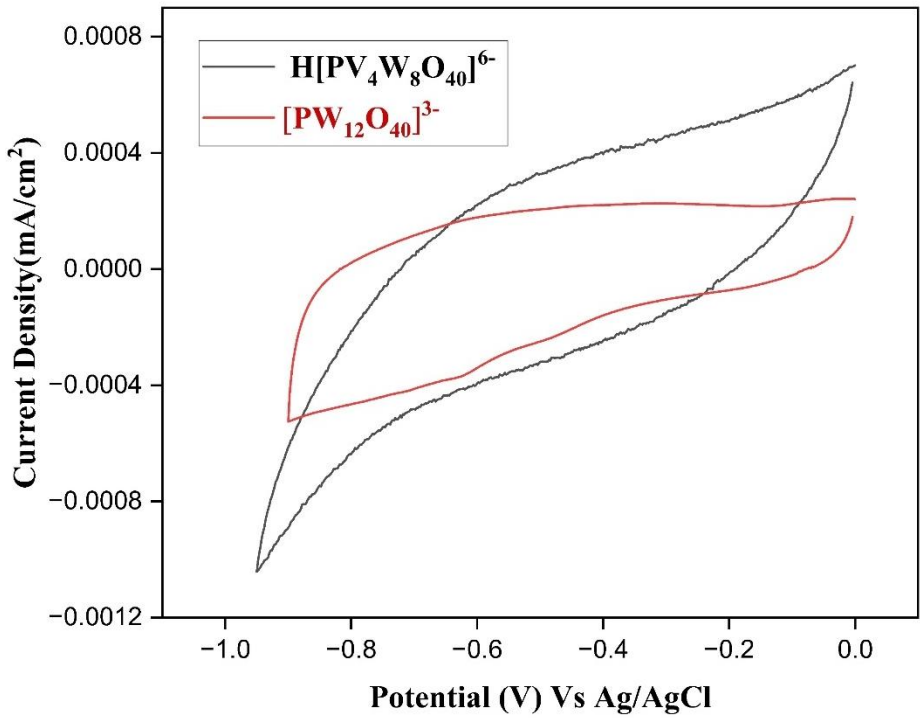

Figure 3.8: Cyclic Voltammetry comparison between $(NH_4)_6H[PV_4W_8O_{40}]$ and $H_3[PW_{12}O_{40}]$

d) Comparison between $H_6[PV_3Mo_9O_{40}]$ and $H_3[PMo_{12}O_{40}]$

The curve suggests the pseudocapacitive behavior of the two compounds but we can observe that $H_6[PV_3Mo_9O_{40}]$ shows better areal capacitance in comparison to $H_3[PMo_{12}O_{40}]$, which is due to the incorporation of vanadium atoms into the structure, which thereby enhances the redox activity of the compound [**Figure 3.9**]. From the area under the curve, it is observed that at 100mV/shas a better areal capacitance of 7.64 mF/cm^2 in comparison to $[PMo_{12}O_{40}]^{3-}$, which has an areal capacitance of 4.81 mF/cm^2 is due to the incorporation of the V atom in the compound.

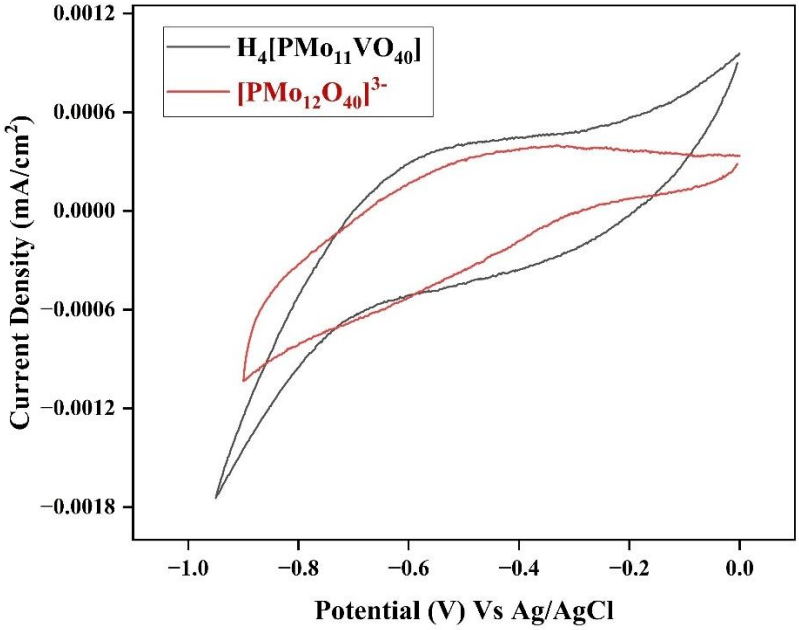

Figure 3.9: Cyclic Voltammetry comparison between $H_6[PV_3Mo_9O_{40}]$ and $H_3[PMo_{12}O_{40}]$

3.3.2 Galvanostatic charge discharge studies

Galvanostatic charge discharge studies were used to evaluate the energy storage performance of the materials. GCD measures capacitance under controlled current conditions. During this, a current pulse was given to the working electrode and potential was measured as a function of time against reference electrode.

From such studies, areal capacitance values were calculated using the formula,

$$C = \frac{2 * I * t}{V * A}$$

a) $(NH_4)_6H[PV_4W_8O_{40}]$

For $(NH_4)_6H[PV_4W_8O_{40}]$, the triangular nature of the curve suggests the pseudocapacitive nature of the compound [**Figure 3.10**]. The highest areal capacitance was calculated as 168.96 mF/cm^2 at 0.4 mA current, respectively, as presented in the **Table 3.3** presented below.

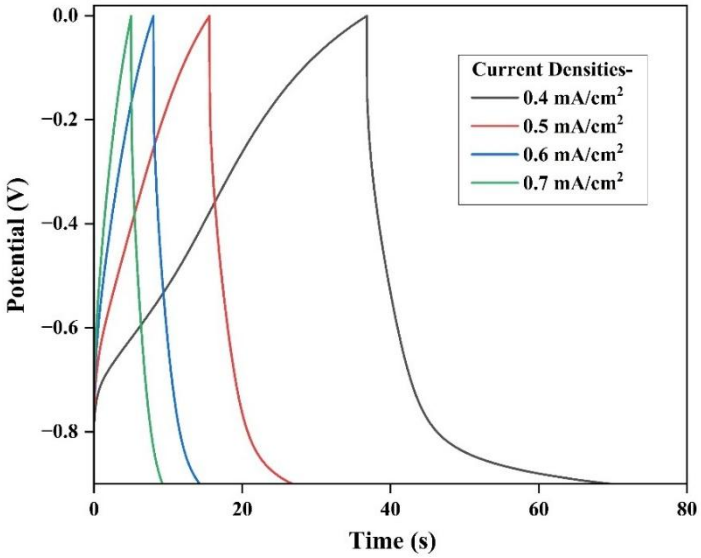

Figure 3.10: GCD Curve for $(NH_4)_6H[PV_4W_8O_{40}]$

Table 3.3: Calculation of areal capacitance for $(NH_4)_6H[PV_4W_8O_{40}]$

Current (mA)	Area (cm^2)/10^{-4}	Potential Window (V)	Capacitance (mF/cm^2)
0.4	76.24528	0.95	168.9646
0.5	21.71611	0.95	48.12435
0.6	9.236895	0.95	20.46957
0.7	4.92861	0.95	10.92213

b) $H_6[PV_3Mo_9O_{40}]$

For $H_6[PV_3Mo_9O_{40}]$ also, the triangular nature of the curve suggests the pseudocapacitive nature of the compound [**Figure 3.11**]. The highest areal capacitance is calculated as 160.10 mF/cm^2 at 0.4 mA current, respectively, as presented in the **Table 3.4** presented below.

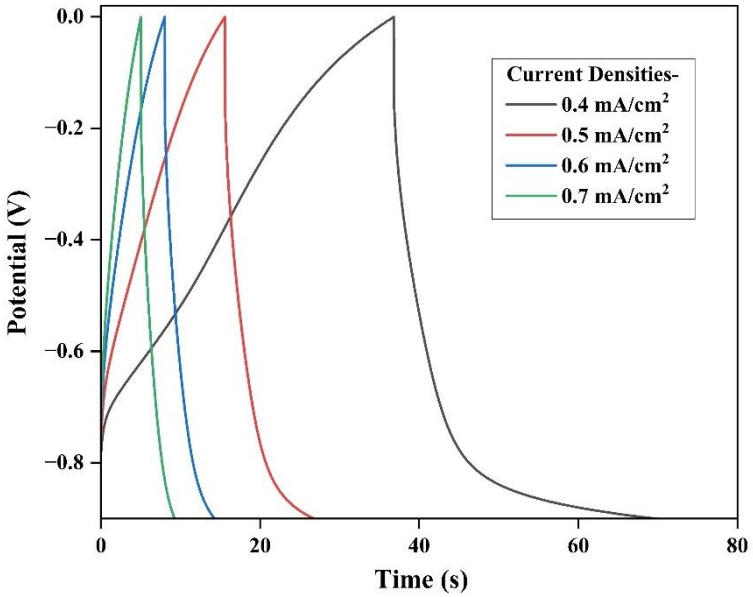

Figure 3.11: GCD Curve for $H_6[PV_3Mo_9O_{40}]$

Table 3.4: Calculation of areal capacitance for $H_6[PV_3Mo_9O_{40}]$

Current (mA)	Area $(cm^2)/10^{-4}$	Potential Window (V)	Capacitance (mF/cm^2)
0.4	72.24528	0.95	160.1003
0.5	20.71611	0.95	45.90828
0.6	10.23689	0.95	22.68564
0.7	6.92861	0.95	15.35426

3.3.3 Electrochemical Impedance Spectroscopic studies

Electrochemical Impedance Spectroscopic studies were used to analyze the interfacial properties of electrified interfaces. The graph a is a Nyquist plot, representing the frequency response of the system. The curve suggests both capacitive and resistive elements contribute to the overall impedance.

a) $(NH_4)_6H[PV_4W_8O_{40}]$

The measured and calculated data points are very close to each other. This indicates that the chosen equivalent circuit model effectively. **Figure 3.12(b)** is the Bode plot where the phase angle is around 25 degrees. This means that the output signal is shifted by 25 degrees relative to the input signal $(NH_4)_6H[PV_4W_8O_{40}]$.

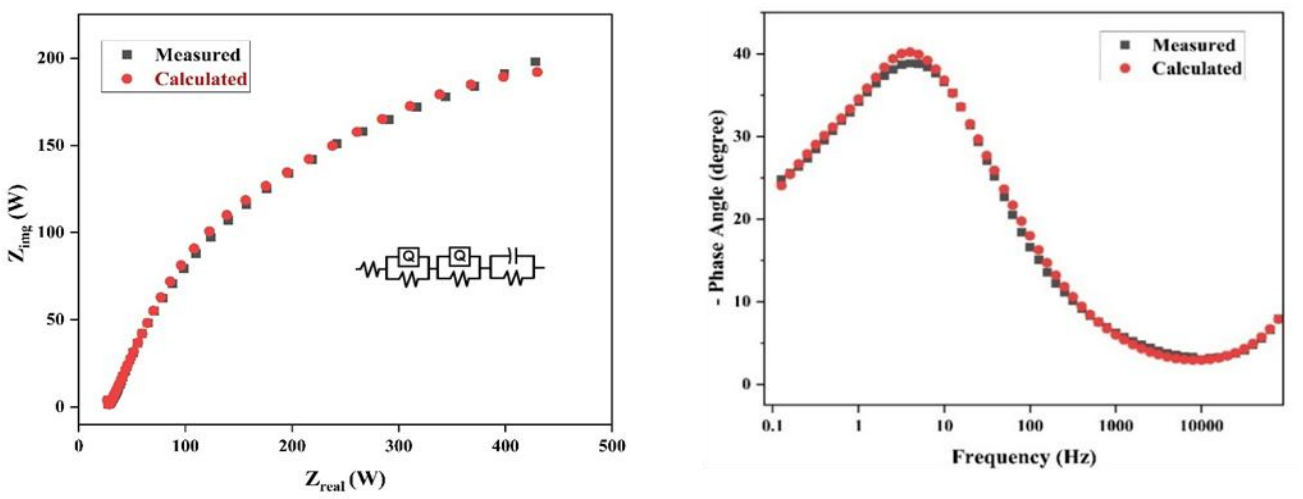

(a) **(b)**

Figure 3.12: a) Nyquist Plot and b) Bode Plot for $(NH_4)_6H[PV_4W_8O_{40}]$

b) $H_6[PV_3Mo_9O_{40}]$

The measured and calculated data points are very close to each other. This indicates that the chosen equivalent circuit model effectively. **Figure 3.13(b)** is the Bode plot where the phase angle is around 23 degrees. This means that the output signal is shifted by 23 degrees relative to the input signal.

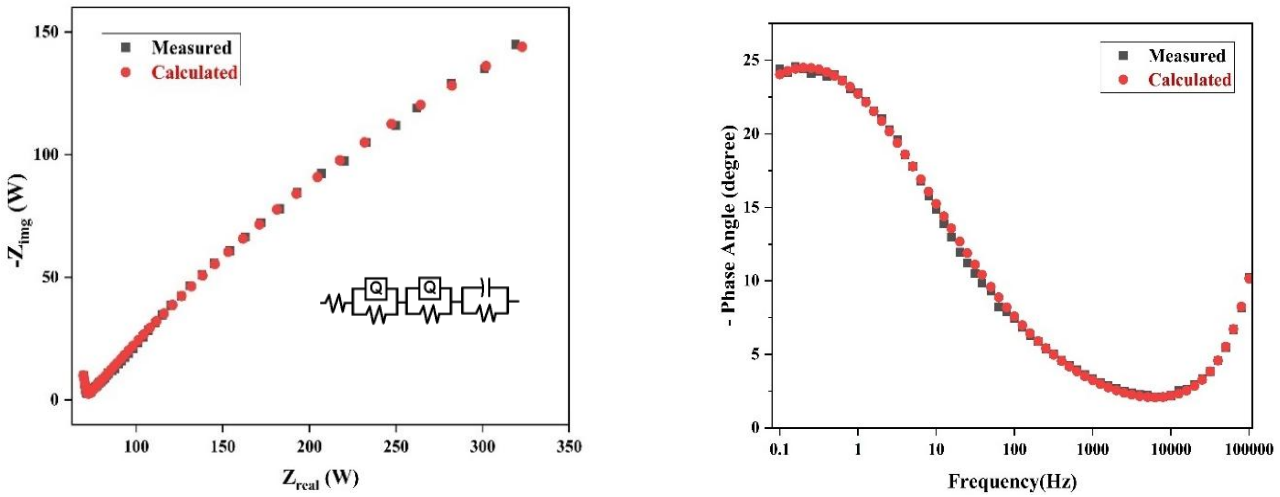

(a) **(b)**

Figure 3.13: a) Nyquist Plot and b) Bode Plot for $H_6[PV_3Mo_9O_{40}]$

CHAPTER 4: CONCLUSION

4. Conclusion

This study conclusively demonstrates the positive impact of vanadium incorporation into Keggin-type polyoxometalates on their electrochemical performance. The vanadium-substituted derivatives $H_6[PV_3Mo_9O_{40}]$ and $(NH_4)_6H[PV_4W_8O_{40}]$, exhibited notable improvements in both structural integrity and functional electrochemical characteristics.

Infrared spectroscopy confirmed the successful integration of vanadium through the appearance of characteristic V=O and O–V–O vibrational modes in the range of 955–930 cm^{-1} and ~820 cm^{-1}, respectively. UV-Visible spectra also validated structural modification, with shoulder peaks at 360 nm for $H_6[PV_3Mo_9O_{40}]$ and 362 nm for $(NH_4)_6H[PV_4W_8O_{40}]$, absent in the parent compounds, indicating altered charge transfer dynamics due to vanadium incorporation.

Electrochemical studies further established superior capacitive behavior in the vanadium-substituted compounds. From cyclic voltammetry, and $(NH_4)_6H[PV_4W_8O_{40}]$ achieved a maximum areal capacitance of 56.88 mF/cm^2 at 5 mV/s, outperforming its parent compound and $H_3[PW_{12}O_{40}]$, which only reached 6.89 mF/cm^2 at 100 mV/s. Similarly, $H_6[PV_3Mo_9O_{40}]$ reached 51.79 mF/cm^2, higher than $H_3[PMo_{12}O_{40}]$'s 4.81 mF/cm^2. Galvanostatic charge-discharge studies echoed these trends, with $(NH_4)_6H[PV_4W_8O_{40}]$ and $H_6[PV_3Mo_9O_{40}]$ reaching maximum capacitances of 168.96 mF/cm^2 and 160.10 mF/cm^2, respectively, at 0.4 mA current. Electrochemical impedance spectroscopy (EIS) provided further support for the enhanced electrochemical behavior, with both compounds showing favorable Nyquist and Bode plots. Phase angles of 25° for $(NH_4)_6H[PV_4W_8O_{40}]$ and 23° for $H_6[PV_3Mo_9O_{40}]$ confirmed fast ion diffusion and stable electrochemical interfaces.

Overall, this work establishes vanadium-substituted oxo-tungstates and oxo-molybdates as promising materials for high-performance energy storage applications.